**CHAPTER 6**

# DESIGN AND PIC SIMULATION OF THE BI-FREQUENCY MILOs*



*Part of this work has been published as:

**Arjun Kumar,** Prabhakar Tripathi, Smrity Dwivedi, and P. K. Jain, "PIC Simulation Study of L-band Bifrequency Magnetically Insulated Line Oscillator," *IEEE URSI Asia-Pacific Radio Science Conference (AP-RASC)*, pp. 1-4, 2019.

## 6.1. Overview

In this chapter, the design and PIC Simulation of different bi-frequency MILO has been explained in detail. There are basically two different kinds of designing procedure which are used to generates bi-frequency through a single MILO device. The first kind uses azimuthal partition of interaction structure whereas the second kind uses axial partition of the RF interaction structure. In the azimuthal partition interaction structure which also has axially periodic disc loading in coaxial waveguide structure, the two different interaction cavity depths formed along the two sections azimuthally that are mainly capable of bi-frequency generation. The theory has been explored in the previous chapters. The maximum frequency difference which can be achieved through this kind of design is ~300 MHz. In axial partitioning of interaction structure, two different cavity depths responsible for RF generation in two different bands which are separated by a segregation cavity. Here in this chapter, the simulation study of azimuthal partitioned bi-frequency MILO has been done which is generating RF at frequencies in *L*-band (i.e. 1.31 GHz and 1.53 GHz) and *S*-band (i.e. 3.4 GHz and 3.65 GHz). Along with this, the simulation study of a dual-band MILO which generates RF in *S*-band and *Ku*-band has been presented in this chapter. The standard device design methodology has been followed with tuning the cavity depth in azimuthal direction for the design of two different and stable frequencies and validated through simulation. Similarly, for dual-band MILO the design parameters and the region of operation have been calculated through the convention MILO device design methodology. The dispersion diagram for both *L*-band and *S*-band bi-frequency has been calculated through eigenmode simulation. For the PIC simulation of the device, different beam parameters for both the design has

been taken and the overall power efficiency of ~8% for *L*-band bi-frequency and ~6.5% for *S*-band bi-frequency has been achieved through the devices. For dual-band MILO, the analytical study of beam-wave interaction inside the two different interaction structure (SWS1 and SWS2) has been presented here with the temporal growth rate calculation at two different frequencies. The dispersion diagram for both *S*-band and *Ku* -band has been calculated through eigenmode simulation and found in close agreement with the analytical results. For the PIC simulation of the device, typically selected beam parameters: diode voltage of 610 kV and diode current of 58 kA, generates the RF of 3.1 GW at frequency 14 GHz (i.e. in *Ku*-band) and RF of 1.2 GW at frequency 2.1 GHz (i.e. in *S*-band). The overall efficiency of ~12.1 % has been achieved with a frequency difference of ~8.4 dB for this dual-band MILO.

## 6.2. Introduction

High power microwave devices that are capable of generating dual frequencies have generated lot of research interest in the recent years [Benford *et al.* (2007)]. Potential applications of such devices are in plasma heating, large-range energy transmission, linearly charged particle accelerators, and electronic warfare systems [Tang *et al.* (2012)]. Various HPM sources developed in recent years to generate dual frequency are mainly Relativistic Backward Wave Oscillator (RBWO), Magnetically Insulated Line Oscillator (MILO), Cerenkov Oscillator and Transit Time Oscillator (TTO) [Yang *et al.* (1999), He *et al.* (2011) and Ju *et al.* (2014)]. Among these devices, MILO attracts the researcher due to its self-magnetic insulation, compact size, and lightweight features [Lemke *et al.* (1997)].

The dual-frequency generation via the HPM source mainly uses two types of

design methodology. The first type of design method uses the concept of two different HPM devices in a single device. Yang *et al.* first proposed a dual-frequency Cherenkov oscillator considering RBWO and the relativistic Orotron concept in a single device [Yang *et al.* (1999)]. The proposed device had used a T-type of structure and the output microwave was taken out perpendicular to each other. Zhang *et al.* reported experimentally using the MILO and virtual cathode oscillator (VCO) concept in a single device that the device generates three frequencies (i.e. 2.1 GHz, 3.8 GHz, and 4.1 GHz) with an overall efficiency of ~ 13.44% [Zhang *et al.* (2015)]. Xiao *et al.* reported simulation work by using the concept of coaxial TTO and MILO in a single device which generates RF power in three frequencies with an overall efficiency of 25.4% [Xiao *et al.* (2009)]. The use of different device concepts in a single device makes the design more complex and RF extraction becomes very difficult.

The second type of design method uses two different interaction structures which are separated either axially or azimuthally. Chen *et al.* reported experimentally an azimuthally partitioned bi-frequency MILO which generates 620 MW of RF power in L-band at two frequencies (i.e. 1.27 GHz and 1.49 GHz) with an overall efficiency of 4.3% [Chen *et al.* (2009)]. Azimuthally partitioning of the interaction structure produces asymmetric modes inside the device which causes a drop in overall device efficiency. Tang *et al.* designed *X*-band dual-frequency coaxial RBWO with frequencies of 10.06 GHz and 10.46 GHz with a conversion efficiency of 16.1% [Yang *et al.* (1999)]. Jin-Chuan *et al.* have used two different interaction structures (i.e. which are separated by a baffle cavity) in a single MILO device and reported RF power generation in *C*-band and *X*-band with an efficiency of 11.8% [Jin *et al.* (2009)]. J-C Ju *et al.* have designed dual-band MILO with frequencies of 1.72 GHz and 14.6 GHz (*L*/*Ku*-band) with a conversion

efficiency of 12.8% [Ju *et al.* (2014)]. But such literature lacks proper interpretation of device design methodology and proper analysis to support device beam-wave interaction mechanisms. To bridge this literature gap, the dual-band MILO device is designed with a defined device design methodology and beam-wave interaction analysis in this chapter. The MILO device can generate dual-frequency (i.e. in *S*-band and *Ku*-band) using two separate interaction structures. The generation of *S*-band and *Ku*-band microwave through a single device shows high $pf^2$ factors with *f* and *p* respectively denotes microwave frequency and microwave power [Ju *et al.* (2014)].

In this chapter, the device design parameters and oscillation conditions for bi-frequency MILO are derived in section 6.3. Section 6.4 explains the simulation of the different bi-frequency MILO which include cold simulation and PIC simulation of L-band and S-band bi-frequency MILO along with S/Ku dual-band MILO. Finally, the conclusion of this chapter is presented in section 6.5.

## 6.3. Design Procedure of the Bi-frequency MILOs

The design of a Bi-frequency or dual-band MILO starts with a selection of bands in which the RF should be generated. The cathode radius ( $r_c$ ) is generally considered as the design normalization parameter. The first design parameter, disc inner radius (i.e. $r_d$) is selected here for calculation. The ratio of disc inner radius and cathode radius (i.e. $r_d / r_c$) is calculated using the input anode current ( $I_a$ ) and the expression is given as [Lemke *et al.* (1997)]:

$$I_a = \frac{I_\alpha}{\ln\left(r_d / r_c\right)} \gamma_a \ln\left(\gamma_a + \sqrt{\gamma_a^2 - 1}\right) \quad , \qquad (6.1)$$

where, $I_\alpha = 8.5$ kA and $\gamma_a = 1 + V_0 / 511$. The interaction cavity for two different frequencies desired in the same band or different band is designed generally for π-mode of operation and the depth of the resonant cavity is considered as λ/4. Thus the outer anode radius can be designed as [Ju *et al.* (2009)]:

$$r_a = r_d + \lambda / 4 \quad , \tag{6.2}$$

where, λ is the operating wavelength. The choke radius ($r_{ch}$) is selecting such that the cut-off frequency of the choke section become ~80% of the operating frequency for the different band of the device [Kumar *et al.* (2019)]. Similarly, the extractor radius ($r_E$) should be selected such that it helps in matching the impedance between the interaction section and the output section of the device [Lemke *et al.* (1997)]. For the given input voltage ($V_0$) and current ($I_a$), the drift velocity ($v_e$) of electron between the anode and cathode structure is calculated as [Dwivedi and Jain (2013), and Cousin (2005)]:

$$v_e = \frac{2\pi\varepsilon_0 c^2}{\ln(r_a / r_c)} \frac{V_0}{I_a} \quad , \tag{6.3}$$

where, $c$ is the speed of light. The efficient beam-wave interaction occurs by selecting accurate disc loading periodicity ($L$). The beam wave interaction starts when the phase velocity (i.e. $v_p$) of the desired mode becomes equal to the drift velocity of the electron. The phase velocity can be calculated as [Dwivedi and Jain (2013), and Cousin (2005)]:

$$v_p = \omega / \beta_0 = 2Lf \quad , \tag{6.4}$$

where, $\beta_0$ is the phase constant. The self-magnetic insulation inside the MILO is the crucial factor of the designing and it develops due to the DC current generated inside the

device. The required magnetic field generates when the DC current becomes greater than or equal to the critical current (i.e. $I_{cr}$) which is calculated as [Lemke *et al*. (1997), and Cousin (2005)]:

$$I_{cr} = \frac{4\pi m_0 c^3 \varepsilon_0 \sqrt{\gamma_a^2 - 1}}{e \ln(r_a / r_c)} \quad , \tag{6.5}$$

where, $m_0$ and $e$ are the mass and charge of an electron, respectively, and $\varepsilon_0$ is the permittivity. This critical current (i.e. $I_{cr}$) generates the cut-off magnetic field (i.e. $B_c$) which is calculated as [Cousin (2005)]:

$$B_c = \frac{\mu_0 I_{cr}}{2\pi r_c \ln(r_a / r_c)} \quad . \tag{6.6}$$

After the calculation of the magnetic field, it becomes important to verify the region of operation of the device. The region of operation is defined between the Hull cut-off voltage (i.e. $V_H$) and threshold voltage (i.e. $V_{BH}$) which can be found by these expressions [Cousin (2005)]:

$$V_H = \frac{m_0 c^2}{e}\left(\left[1 + \left(\frac{eB_\theta r_d}{m_0 c}\right)^2\right]^{1/2} - 1\right) \tag{6.7}$$

and

$$V_{BH} = B_\theta r_d v_\phi - \frac{m_0 c^2}{e}\left[1 - \left(1 - \frac{v_\phi^2}{c^2}\right)^{1/2}\right] \quad . \tag{6.8}$$

The design of the segregation cavity is considered as one of the most important parts of any dual-frequency device. The single band bi-frequency MILO does not require any

segregation cavity as the two frequencies generated inside such MILO device are in the same band and their frequency difference is not very high. The depth and length of the segregation cavity are selected according to the next higher-order mode (i.e. $TM_{02}$ mode) of the main operating mode (i.e. $TM_{01}$ mode) of the device. The segregation cavity oscillates toward the higher-order mode (i.e. $TM_{02}$ mode) and cut-off the main operating mode (i.e, $TM_{01}$ mode) in such a way that it reflected back in the forward direction (i.e. in the direction of propagating wave). The cavity radius ($r_w$) of the segregation cavity is calculated as [Davis and Gibson (2006)]:

$$r_w = \frac{\chi_{np} c}{2\pi f_r} \quad , \tag{6.9}$$

where, $f_r$ is the resonating frequency and $\chi_{np}$ is the modal root of the n$^{th}$ order Bessel–Neumann combination defined as [Lemke (1989)]:

$$J_n(k_c r_c) Y_n(k_c r_w) - J_n(k_c r_c) Y_n(k_c r_w) = 0 \quad . \tag{6.10}$$

Finally, using the above describe expressions one can calculate the design parameters for desired frequencies either in single band or dual-band.

## 6.4. PIC Simulation of the Bi-frequency MILOs

A simulation study of bi-frequency MILO is mainly considered to validate the theory of generation of two different frequencies using a single device. Simulation of an HPM device is done in two steps. In the first step, the device design parameters obtained through design expressions are validated in the absence of an electron beam called the cold simulation. The cold simulation gives information about the operating frequency and desired mode of operation supported by the RF interaction structure. After the cold

simulation, beam present simulation (adapting PIC simulation) is performed to evaluate the RF generation capacity through the device. If the generated RF signal and efficiency obtained through simulation is not satisfactory then the optimization of design parameters is redone through a different optimization technique. Here, a detailed simulation study of bi-frequency MILO has been performed for *L*-band generating frequencies of 1.31 GHz and 1.53 GHz, for S-band generating frequencies of 3.4 GHz and 3.65 GHz, and for S/Ku dual-band generating frequencies of 2.1 GHz and 14 GHz.

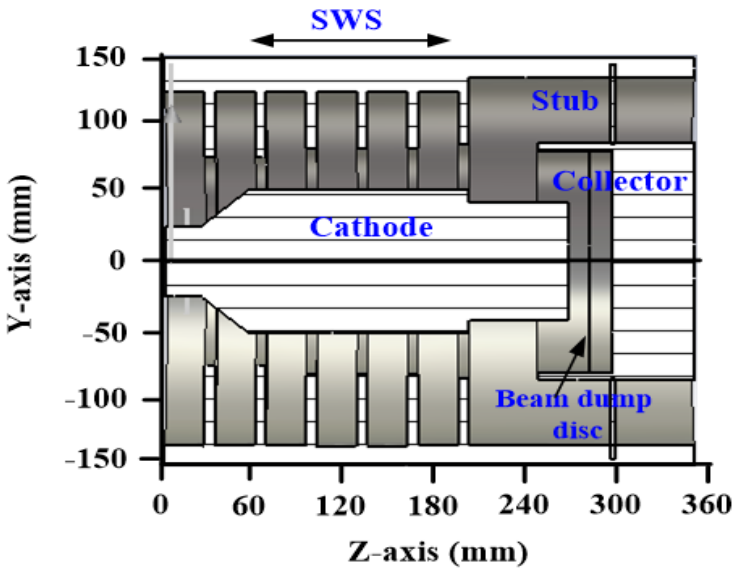


**Figure 6.1:** The typical schematic of azimuthal partition *L*-band bi-frequency MILO.

### 6.4.1 *L*-band Bi-frequency MILO

A detailed PIC simulation of BFMILO followed by cold simulation is performed here for *L*-band generating frequencies of 1.31 GHz and 1.53 GHz. The design parameters are calculated using the above described expression given by Eqs. (6.1) to (6.10) is presented in Table 6.1 and validated through beam absent simulation (cold simulation), which helps in obtaining the operating frequency and modes for the device through dispersion

characteristics and field patterns, respectively. Further, beam present simulation is performed for explaining the beam-wave interaction and RF output power developed in the device followed by modification in the collector design for performance improvement.

**Table 6.1:** Design Specification of *L*-band bi-frequency MILO [Chen *et al.* (2009)]

| **Particulars** | **Specifications** |
|---|---|
| Voltage | 420kV |
| Current | 38kA |
| Cathode Radius ($r_c$) | 55 mm |
| Anode Radius ($r_w$) | 129 mm, 140 mm |
| SWS Disc Radius ($r_d$) | 86 mm |
| Extractor Disc Radius | 90 mm |
| Choke Disc Radius | 80 mm |
| Disc Thickness ($T$) | 7 mm |
| Periodicity ($L$) | 34 mm |

Fig. 6.1 shows the typical schematic of azimuthal partition bi-frequency MILO. The design methodology follows a similar procedure as the conventional MILO with two choke discs at the input side, three SWS discs of radius $r_d$, extractor disc, the cathode of radius $r_c$, collector, and stub. Azimuthal partition at $180^0$ forms two different cavity depths $r_{w1}$ and $r_{w2}$. Step ladder cathode designed in this device for better magnetic insulation and beam wave interaction.

## Cold Simulation (Beam absent simulation)

The beam absent simulation of the azimuthal partition unit cavity structure is performed using the device design parameters given in table 6.1. The eigenmode solver of 'CST

Studio Suite' is used for cold test of SWS structure. To define the operating frequency of the device, the dispersion characteristic of the SWS structure is evaluated for different modes. Fig. 6.2 shows the dispersion curve for five different modes. Due to the azimuthal partition of the SWS cavity, asymmetric modes are generated inside the structure. Mode 1 is the fundamental symmetric mode, mode 2 and mode 3 are the degenerate $HEM_{11}$ mode and mode 4 and mode 5 are the degenerate $HEM_{21}$ mode [Wang *et al.* (2010)].

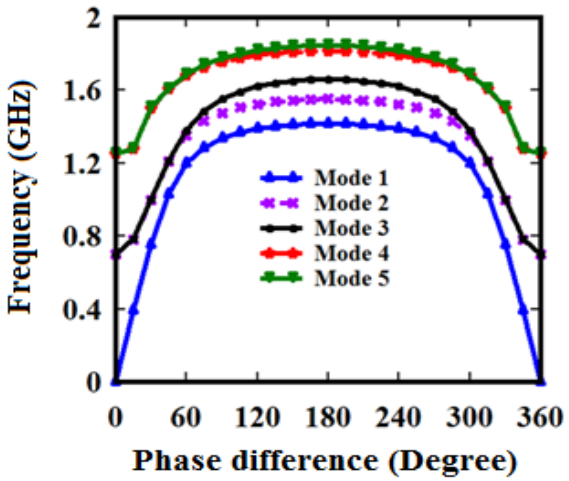


**Figure 6.2**: Dispersion curve for azimuthally non-uniform structure with $r_{w1}$=129 mm and $r_{w2}$=140 mm.

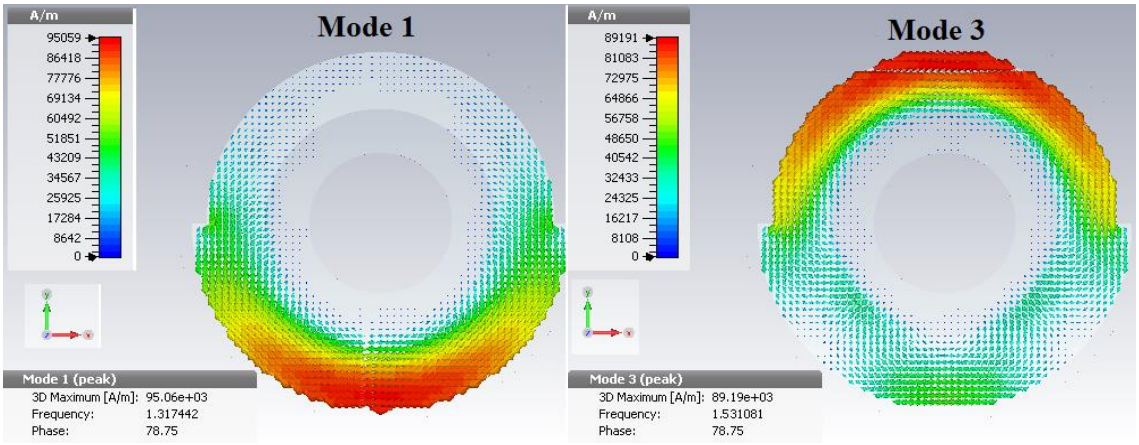


**Figure 6.3:** Magnetic field vector distribution for operating modes: mode 1 and mode 3.

The magnetic field vector distribution of mode 1 and mode 3 shown in Fig. 6.3 explain the maximum field distribution in two different azimuthal partitions [Wang *et al.* (2010)]. In mode 1, the magnetic field distribution is mainly located in the azimuthal cavity of $180^0$-$360^0$. Similarly, the magnetic field distribution of mode 3 is located in the azimuthal cavity of $0^0$-$180^0$. Thus, mode 1 and mode 3 are the operating modes of the BFMILO with the π-mode frequency of 1.31 GHz and 1.53 GHz, respectively.

## PIC Simulation (Beam present simulation)

After the cold simulation, which describes the operating modes and frequency of the structure, beam present simulation is carried out using PIC solver of 'CST Particle Studio'. A high voltage of 420 kV DC pulse is applied between cathode and anode which causes electrons emission from the cylindrical cathode curved surface generating 38 kA current. Emitted electrons initially move radially toward slow-wave structure generating current and after magnetic insulation flow in the axial direction [Lemke *et al.* (1997) and Dixit *et al.* (2017)]. Magnetic insulation is achieved by the device by current called 'critical current'. The critical current required to maintain magnetic insulation can be achieved by load length (cathode projecting inside the collector). The magnetically insulated electron sheath induces noise and generates oscillation at two frequencies when the drift velocity of electrons becomes equal to phase velocity supported by SWS cavities in different azimuthal partition [Chen *et al.* (2009) and Wang *et al.* (2010)]. Fig. 6.4 shows the beam wave interaction of the magnetically insulated electron sheath in two different azimuthal cavities at different time instances. It can be seen from Fig. 6.4 that the beam wave interaction is not azimuthally symmetric which confirms the hybrid modes generation inside the device.

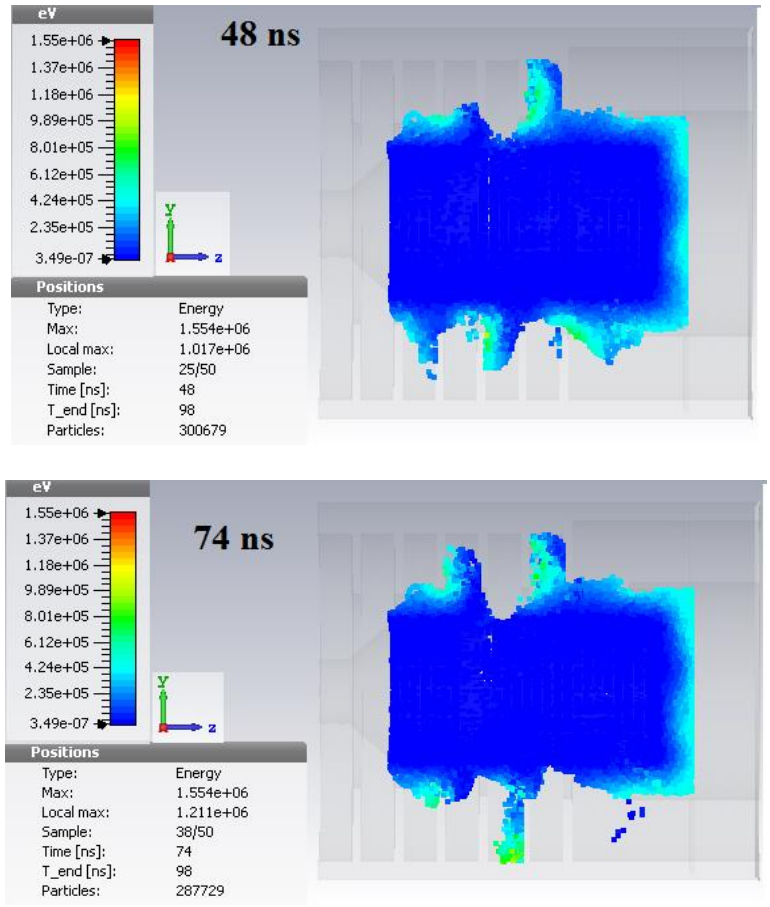


**Figure 6.4:** Phase space of the electron beam at two different time instant at 48 ns and 74 ns to show the asymmetric beam-wave interaction.

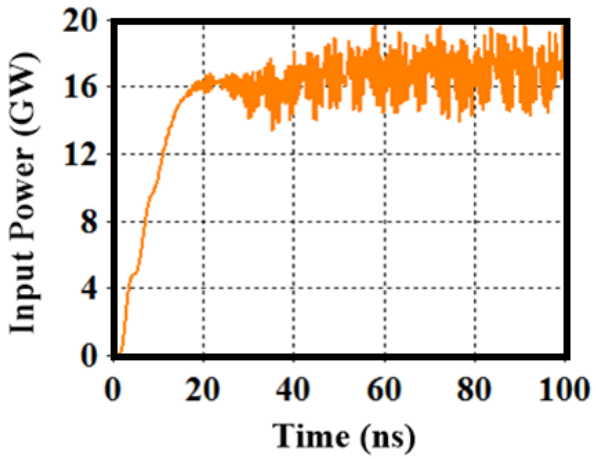


**Figure 6.5:** Temporal wave-particle power transfer with an application of 420 kV of voltage and 38 kA of current.

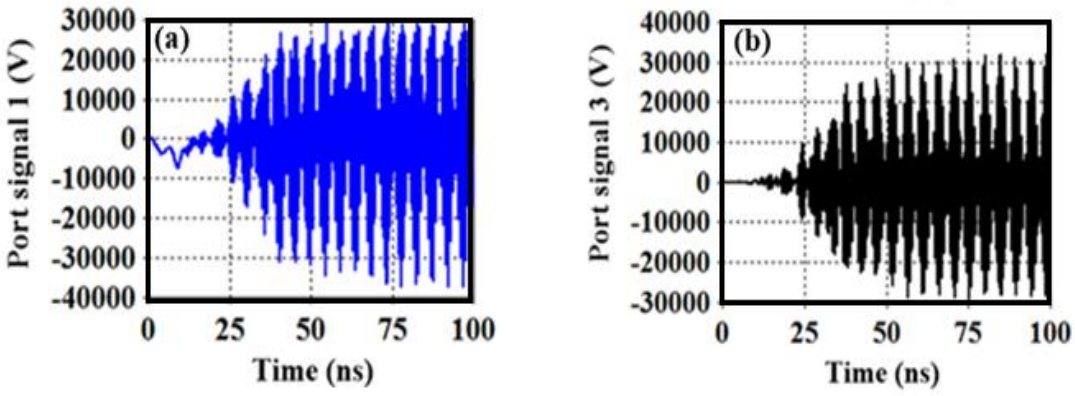


**Figure 6.6:** Temporal RF port signal of (a) mode 1 associated with azimuthal partition $180^0$-$360^0$ (b) mode 3 associated with azimuthal partition $0^0$-$180^0$.

Fig. 6.5 shows the input power of the device after the application of 420 kV of DC voltage at the input side which is ~16.15 GW. A waveguide port is added at the output side of the device to observe the output RF signal at different modes. Fig. 6.6 shows the RF signal generated after beam wave interaction at mode 1 ($TE_{11}$) and mode 3 ($TM_{01}$) with time. The FFT of the voltage signal generated at the output port is shown in Fig. 6.7. It can be observed from this figure that the device operated at two frequencies *i.e.* 1.31 GHz and 1.53 GHz. The drop in the frequency from the cold test to the PIC simulation is due to the beam loading effect.

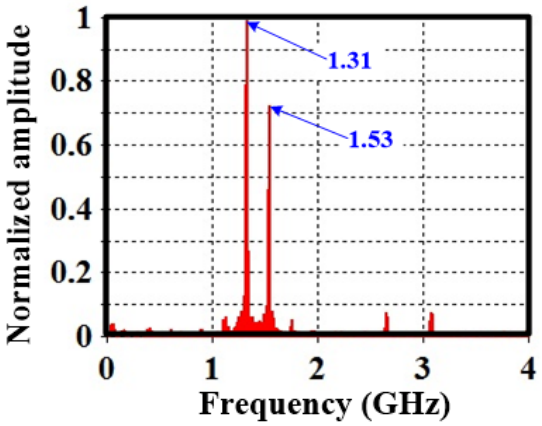


**Figure 6.7:** Frequency spectrum of the generated RF signal observed at the output port.

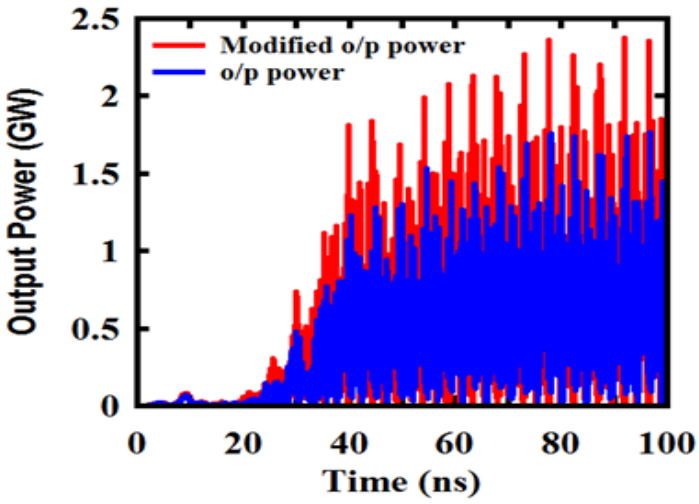


**Figure 6.8:** Combined temporal RF output power of the two modes with and without collector design modification.

After combining the RF signal generated at mode 1 and mode 3, the peak RF output power of 1.29 GW and modified RF output power of 1.59 GW is obtained. Fig. 6.8 shows the combined temporal RF output power of the two modes.

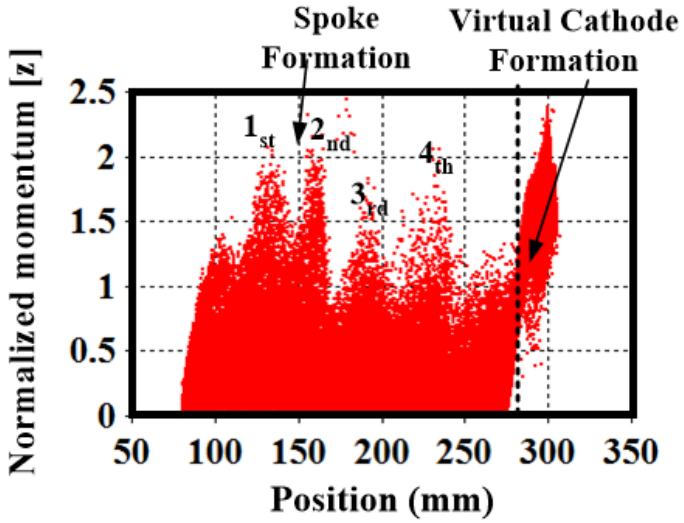


**Figure 6.9:** Virtual cathode formation at the collector through beam dump disc.

Further, to improve the performance of the device, a beam dump disc is used

inside the collector. This beam dump disc accumulates the electrons present inside the collector and helps in the formation of a virtual cathode. The virtual cathode formed inside the collector help to reflect back the bunch of charges towards the SWS cavities for further beam wave interaction [Dixit *et al.* (2017)]. Fig. 6.9 shows the normalized momentum at the different axial positions of the device. It can be seen from the figure that a virtual cathode is formed at the beam dump position with is at 280 mm.

### 6.4.2 *S*-Band Bi-frequency MILO

An involved PIC simulation of bi-frequency MILO which is generating RF in *S*-band with frequencies 3.4 GHz and 3.65 GHz is performed followed by cold simulation. The desired two frequencies can be generated by an azimuthal partition of slow-wave structure which is obtained through designing an anode cylinder with two different inner radii $r_{w1}$ ($0^0$-$180^0$) and $r_{w2}$ ($180^0$-$360^0$). The dual cavity SWS supports an operating mode corresponding to each of the two azimuthal cavity depth. Each mode with an operating frequency to support two stable and separate oscillation frequencies. Fig. 6.10 shows the typical schematic of azimuthal partition bi-frequency MILO. The complete design methodology follows the procedure similar to the conventional MILO with two choke discs at the input side, three SWS discs of radius $r_d$, extractor disc, the cathode of radius $r_c$, collector, and stub. The design parameters for S-band bi-frequency MILO is calculated and presented in Table 6.2 using the above describe expression given in Section-6.3. Azimuthal partition at $180^0$ forms two different cavity depths $r_{w1}$ and $r_{w2}$. Step ladder cathode designed in this device for better magnetic insulation and beam wave interaction. The simulation starts with firstly performing beam absent simulation to obtain the operating frequency and desired modes for the device through dispersion characteristics

and field patterns, respectively. Further, beam present simulation has been performed for explaining the beam-wave interaction and RF output power developed in the device.

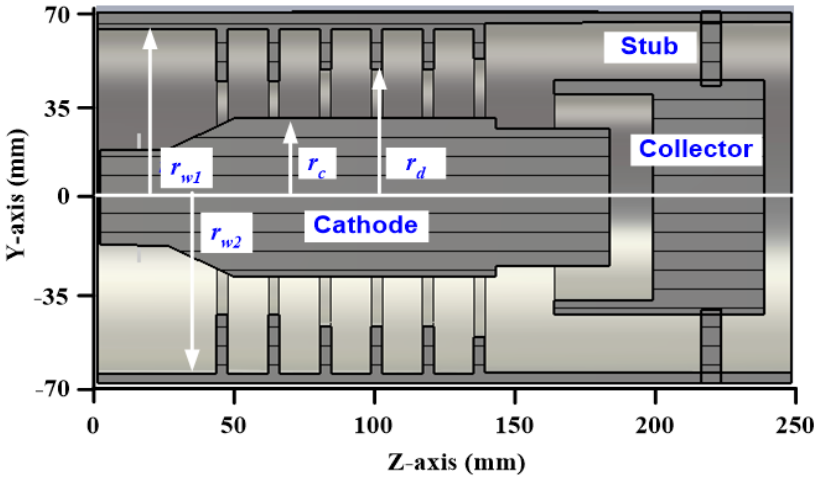


**Figure 6.10:** The typical schematic of azimuthal partition *S*-band bi-frequency MILO.

**Cold Simulations (Beam absent simulation)**

Similar to the *L*-band bi-frequency MILO, cold simulation i.e. the beam absent simulation of the azimuthal partition unit cavity structure for *S*-band bi-frequency MILO is performed using the device design parameters given in Table 6.2. The eigenmode solver of 'CST Microwave Studio' is used for cold test of the interaction structure (i.e. SWS). The dispersion characteristic of the SWS structure is evaluated for different modes to define the operating frequency of the device which is shown in Fig. 6.11. Azimuthal partition of the SWS cavity generates asymmetric modes inside the structure where mode 1 is the fundamental symmetric mode, mode 2 and mode 3 are the degenerate $HEM_{11}$ mode and mode 4 and mode 5 are the degenerate $HEM_{21}$ mode [Wang *et al.* (2010)]. The magnetic field vector distribution of desired modes i.e. mode 1 and mode 3 is shown in Fig. 6.12. It can be seen clearly that two modes are supported by two different azimuthal partitions, not a complete TE or TM mode. In mode 1, the magnetic field distribution is

mainly located in the azimuthal cavity of $0^0$-$180^0$. Similarly, the magnetic field distribution of mode 3 is located in the azimuthal cavity of $180^0$-$360^0$. Thus, mode 1 and mode 3 are the operating modes of the BFMILO with the π-mode frequency of 3.51 GHz and 3.79 GHz, respectively.

**Table 6.2:** Design Parameters of *S*-band bi-frequency MILO [Chen *et al*. (2009)].

| **Particulars** | **Specifications** |
|---|---|
| Voltage | 490kV |
| Current | 45kA |
| Cathode Radius ($r_c$) | 31 mm |
| Anode Radius ($r_w$) | 64 mm, 66 mm |
| SWS Disc Radius ($r_d$) | 48 mm |
| Extractor Disc Radius | 52 mm |
| Choke Disc Radius | 44 mm |
| Disc Thickness ($T$) | 4 mm |
| Periodicity ($L$) | 18.5 mm |

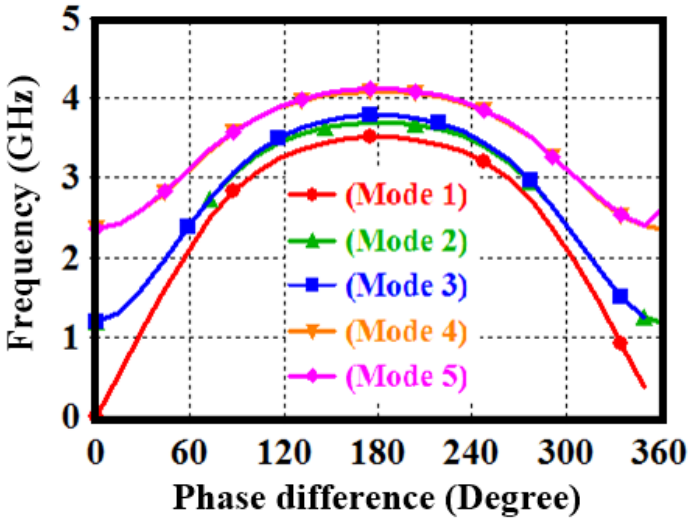


**Figure 6.11:** Dispersion curve for S-band bi-frequency MILO with the azimuthally non uniform structure having $r_{w1}$=64 mm and $r_{w2}$=66 mm.

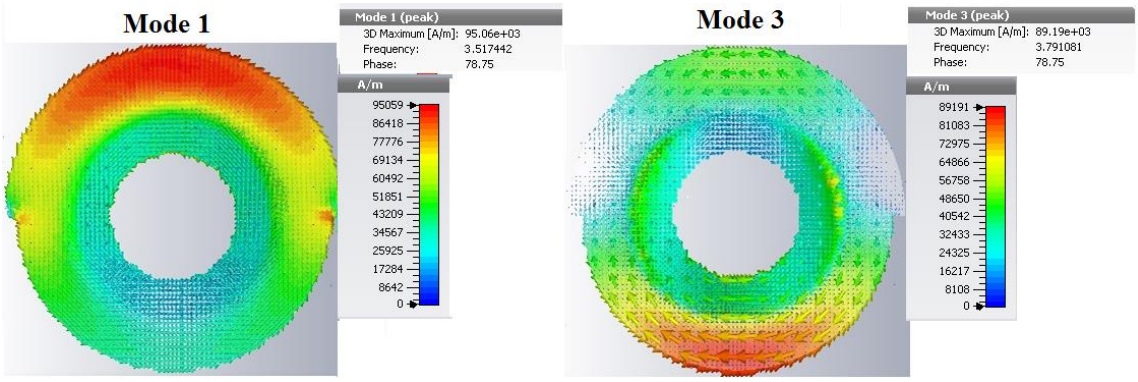


**Figure 6.12:** Magnetic field vector distribution of operating modes (i.e. mode 1 and mode 3) of the S-band bi-frequency MILO.

## PIC Simulation (Beam present simulation)

Similar to the L-band bi-frequency MILO, the PIC simulation of S-band bi-frequency MILO is also performed using the PIC solver of 'CST Particle Studio'. A high voltage of 490 kV DC pulse is applied between cathode and anode which causes electrons emission from the cylindrical cathode curved surface generating 45 kA current. This high current generation inside the device causes magnetic insulation which results in the electron flow in the axial direction. The beam-wave interaction of the magnetically insulated electron sheath in two different azimuthal cavities at different time instances is shown in Fig. 6.13 which confirms the hybrid modes generation inside the device. Fig. 6.14 shows the input power ~22.05 GW of the device after the application of 490 kV of DC voltage and generation of the input current of 45 kA. A waveguide port is added at the output side of the device (with the cylindrical anode) to observe the output RF signal at different modes. Fig. 6.15 shows the temporal RF signal generated after beam-wave interaction in mode 1 and mode 3.

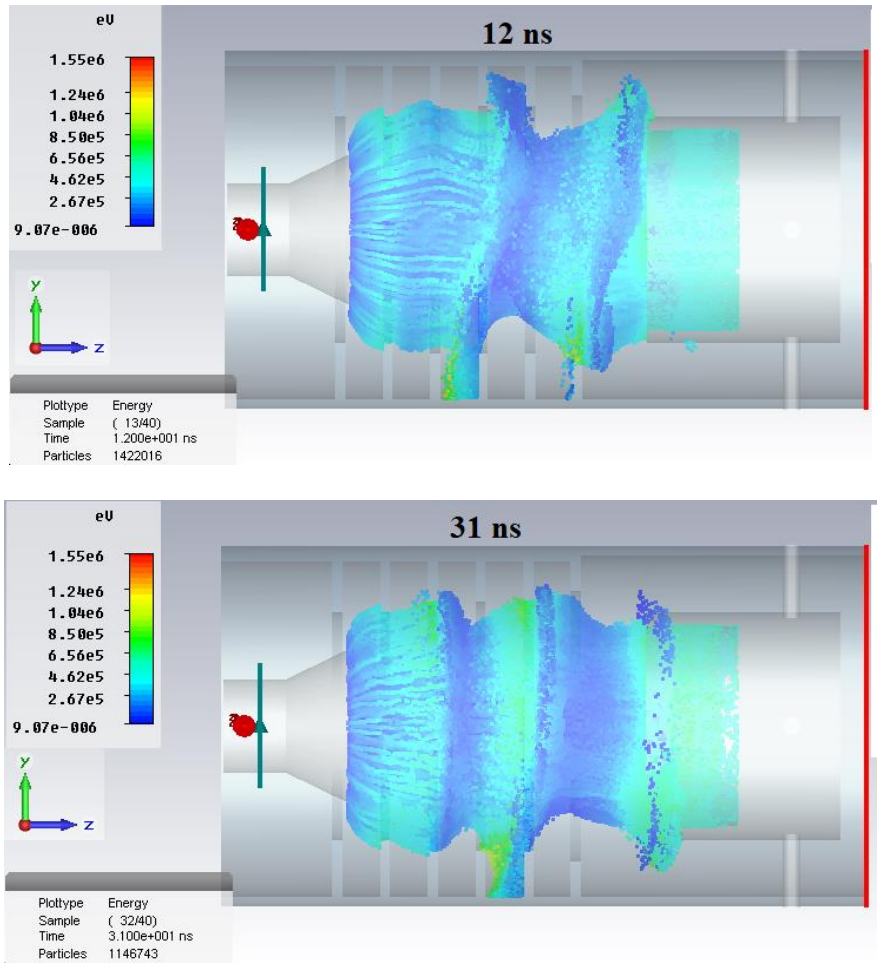


**Figure 6.13:** Phase space of the electron particles for S-band bi-frequency MILO at a different time instant of 12 ns and 31 ns.

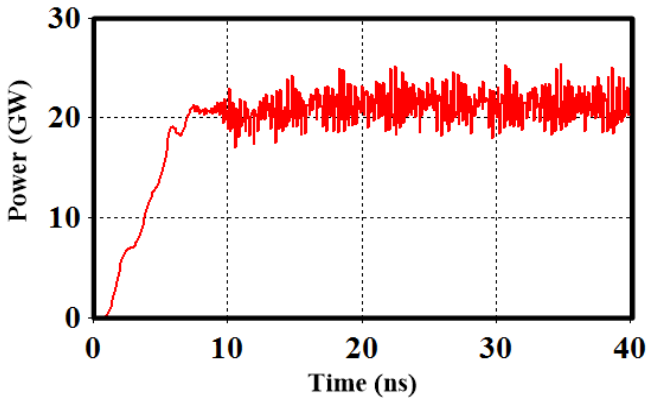


**Figure 6.14:** Temporal input power with the application of 490 kV of voltage and 45 kA of current (also known as wave-particle power transfer).

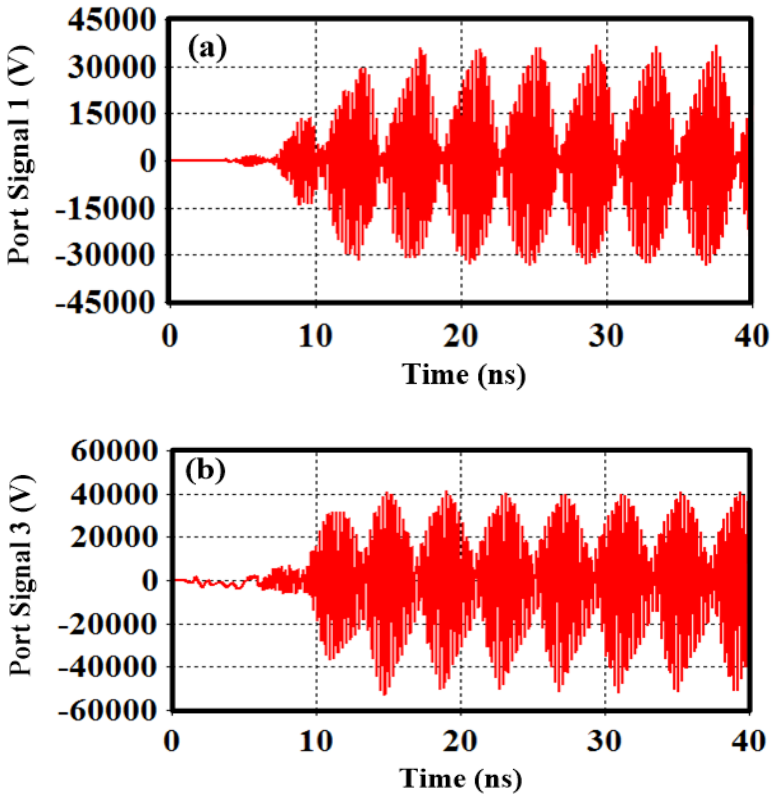


**Figure 6.15:** Temporal RF output port signal of (a) mode 1 (b) mode 3.

The FFT of the voltage signal generated at the output port is shown in Fig. 6.16. It can be observed from the figure that the device operated at two frequencies i.e. 3.4 GHz and 3.65 GHz. The drop in the frequency from the cold test to the PIC simulation is due to the beam loading effect. After combining the RF signal generated at mode 1 and mode 3, the peak RF output power of 2.86 GW, and the average RF output power of 1.43 GW is obtained. Fig. 6.17 shows the combined temporal RF output power of the two modes

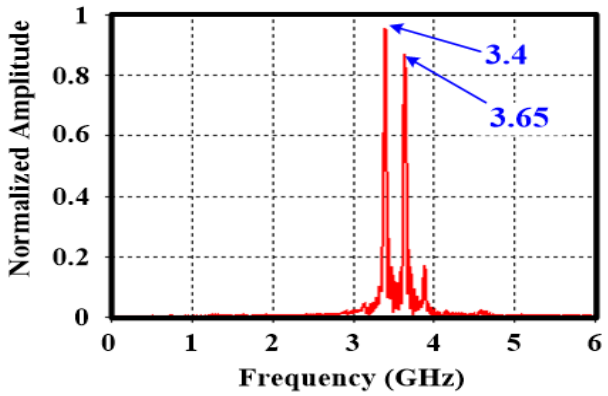


**Figure 6.16:** Frequency spectrum of the RF signal obtained through FFT of the signal obtained at the output port.

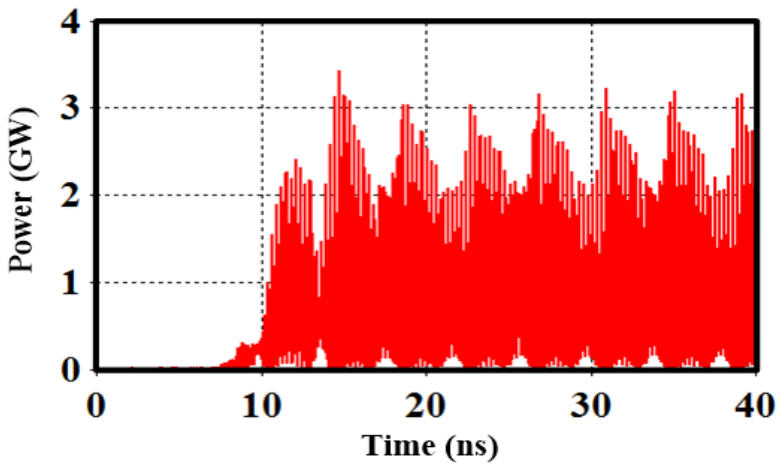


**Figure 6.17:** Combined temporal RF output power of the two frequencies.

### 6.4.3 *S/Ku* Dual-Band MILO

A dual-band MILO is designed for frequencies in *S*-band and *Ku*-band in accordance with different slow-wave structures (i.e. which is form by periodically loaded coaxial disc). The typical schematic of dual-band MILO is shown in Fig. 6.18. The proposed MILO device consists of SWS1 (slow-wave structure) as an anode structure and C1 as a cathode structure for the *S*-band generation section. Similarly, SWS2, C2, and C3 were

used as anode structure, cathode structure (i.e. for the emission of electrons), and the cathode (i.e. for load section), respectively for the *Ku*-band generation section. The self-magnetic insulation occurs inside the device in two phases. In the first phase, magnetic insulation occurs through load current (which starts at the C3 section of cathode) towards the *Ku*-band generation section. In the second phase, the *Ku*-band generation section acts as a load for the *S*-band generation section and creates magnetic insulation inside the whole structure. The RF signals which are generated through efficient beam-wave interaction at the two sections (i.e. in the *S*-band section and *Ku*-band section), can be extracted out through the two different extractor parts. A segregation cavity is used to eliminate the leakage of RF from the lower band (*S*-band) to the higher band (*Ku*-band) and vice-versa. Stub1 and Stub2 here used for DC current feedback in *S*-band and *Ku*-band, respectively.

The dual-band MILO device design methodology follows the structural design parameter explained in the above section 6.3. The calculation of design parameters uses the above design expression given in Eqs. (6.1)-(6.10) and the design parameters are presented in Table 6.3. Two different structure parameters are used for generating frequencies in the different bands. The region of operation for the device is explained using Hull cut-off criteria and Buneman-Hartree criteria shown in Fig. 6.19. The equivalent circuit approach explained in Chapter 5 is used here for investigating the beam-wave interaction for this dual-band MILO. The dispersion relation in presence of electron beam explained the RF generation and propagation inside the different coaxial interaction structures (SWS1 and SWS2) for dual-band MILO device. The imaginary roots of the Eqs. (5.48) given in the previous chapter (i.e. Chapter 5) explain the instability occurs inside the different slow-wave structure due to small plasma

perturbation inside the device and gives the temporal growth rate of the RF generated due to the instability. In the dual-band MILO device, two different interaction structures (i.e. SWS1 for *S*-band and SWS2 for *Ku*-band) are used.

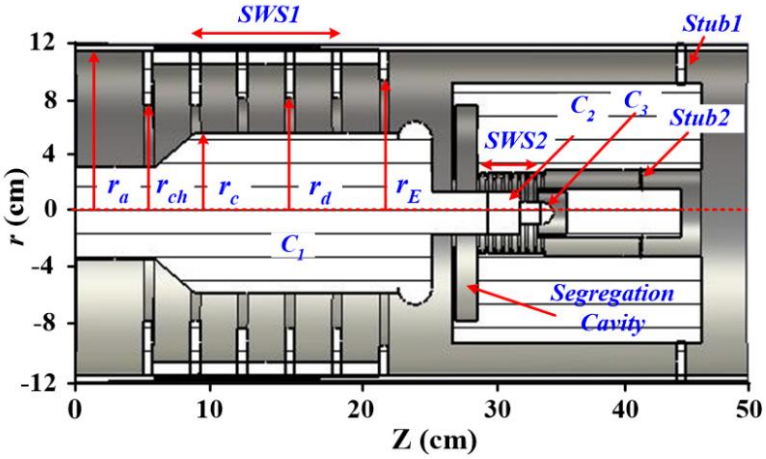


**Figure 6.18:** The typical schematic of dual-band MILO structure with SWS1 and SWS2 as the slow-wave structures, C1, C2, C3 as the cathode.

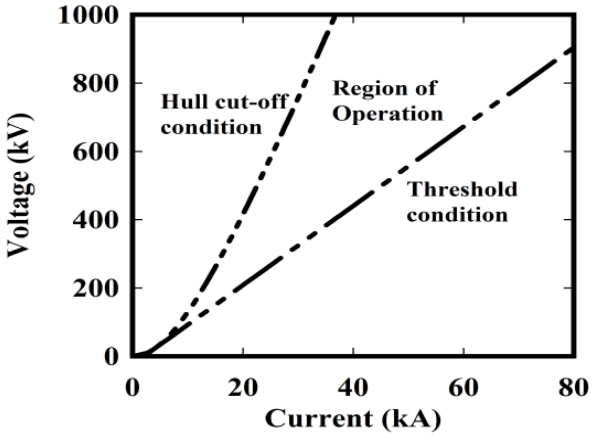


**Figure 6.19:** Region of operation curve defining Hull cut-off condition and Buneman Hartree threshold criteria for the dual-band MILO.

**Table 6.3:** Design Parameters of S/Ku dual-band MILO

| **Particulars** | **Specifications** | |
|---|---|---|
| | **S-band** | **Ku-band [Ju *et al.* (2014)]** |
| Voltage ($V_0$) | 610 kV | |
| Current ($I_a$) | 58 kA | |
| Cathode Radius ($r_c$) | 60 mm | 15.75 mm |
| Anode Radius ($r_a$) | 111 mm | 30 mm |
| SWS disc radius ($r_d$) | 86 mm | 26 mm |
| Extractor disc radius ($r_E$) | 99 mm | 28 mm |
| Choke disc radius ($r_{ch}$) | 80 mm | 24 mm |
| Disc Thickness ($T$) | 7 mm | 2 mm |
| Periodicity ($L$) | 35 mm | 6 mm |

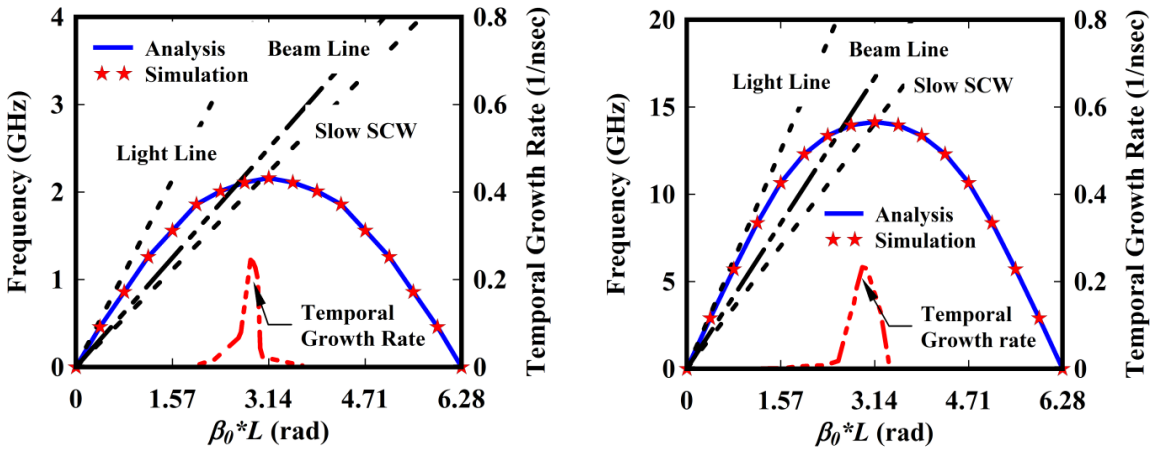


**(a)** **(b)**

**Figure 6.20:** Dispersion curve and its temporal growth rate for the fundamental mode (i.e. $TM_{01}$ mode) (a) of *S*-band and, (b) of *Ku*-band RF interaction structures.

With the design and beam parameters given in Table 6.3, the dispersion curve and temporal growth rate are numerically calculated for different interaction structure. Fig.

6.20 shows the beam present dispersion curve and temporal growth rate for two bands (i.e. for *S*-band and *Ku*-band). The numerically obtained dispersion curve is further verified using the simulation and the results found in good agreement for both the bands (i.e. *S*-band and *Ku*-band). The corresponding beam line and slow space charge line explain the beam-wave interaction range whereas the light line explains that the operation of the device is restricted in the slow-wave region. It can be seen from Fig. 6.20(a) that the instability region for *S*-band lies between phase difference 1.89 rad to 3.17 rad with the maximum temporal growth rate of 0.23 (1/nsec). Similarly, Fig. 6.20(b) explain the instability region for *Ku*-band lies between phase difference 2.5 rad to 3.3 rad with the maximum temporal growth rate of 0.24 (1/nsec). The oscillation frequencies close to π-mode of operation for *S*-band observed ~2.12 GHz and for *Ku*-band ~14.2 GHz which is close to desired frequencies of operation.

**Cold Simulation (Beam absent simulation)**

To validate the structure design the beam absent simulation study of the dual-band MILO device is carried out using Eigenmode solver of 'CST Microwave Studio'. This solver is used to calculate the frequencies corresponding to the phase difference between consecutive discs (dispersion diagram) for both *S*-band and *Ku*-band. Fig. 6.20 shows the dispersion diagram for *S*-band and *Ku*-band calculated through the simulation. It can be seen from Fig. 6.20 that with the design parameter for *S*-band, the frequency of operation for π-mode is ~ 2.2 GHz and for *Ku*-band, the frequency of operation for π-mode is ~ 14.1 GHz, which validate the design parameter of the designed dual-band MILO.

The segregation cavity is used mainly to stop the interference of the generated RF signal at two frequencies. The design of the segregation cavity is explained in section 6.3.

Fig. 6.21 shows the role of the use of the segregation cavity. It can be seen from Fig. 6.21(a) that, the RF signal generated at the SWS1 section (i.e. for the *S*-band generation section) is propagated through extraction section 1 and stopped by the segregation cavity to propagate towards the extractor section 2. Similarly, Fig. 6.21(b) shows that the RF signal generated at the SWS2 section (i.e. for the *Ku*-band generation section) is propagated through extractor section 2 and stopped by the segregation cavity to propagate towards the SWS1 section (i.e. *S*-band generation section).

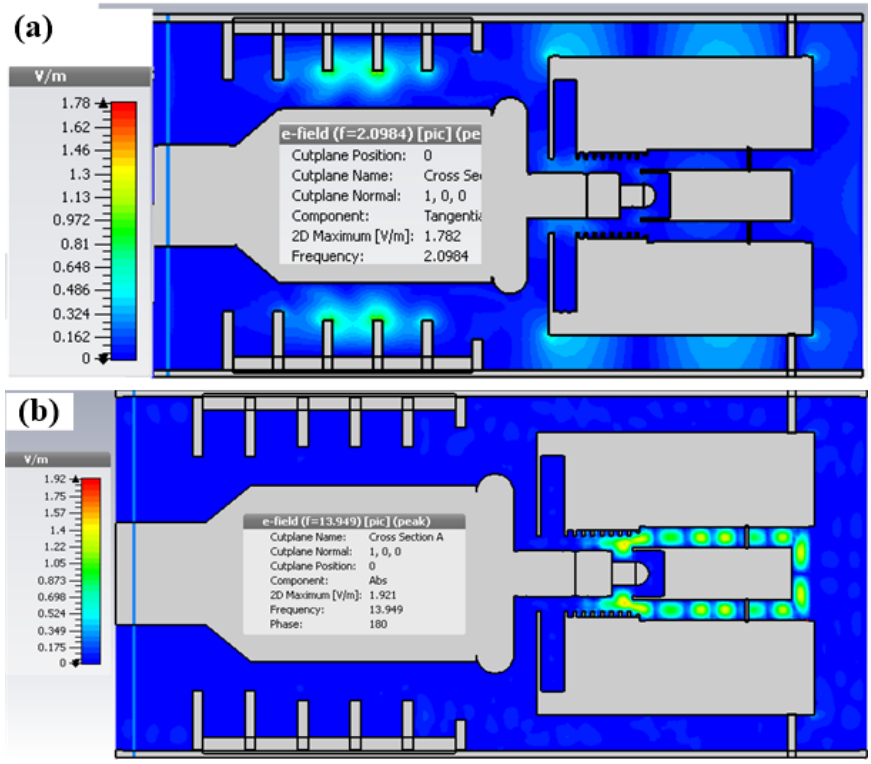


**Figure 6.21:** Role and effect of segregation cavity for different frequency band (a) for *S*-band and, (b) for *Ku*-band.

### PIC Simulation (Beam present Simulation)

Further, the validated designed for dual-band MILO is simulated and optimized using the 3D PIC simulation with the listed structure parameter. The beam present simulation is

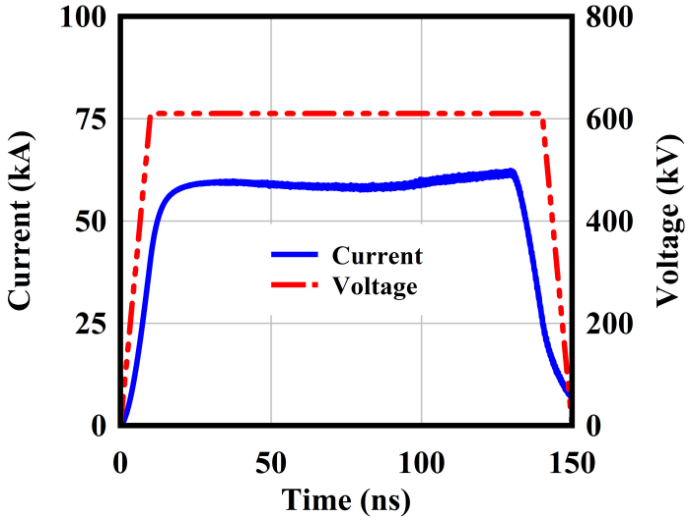


**Figure 6.22:** Applied input DC voltage (in kV) pulse with 10 ns rise time 130 ns hold time and 10 ns fall time with the generated current (in kA).

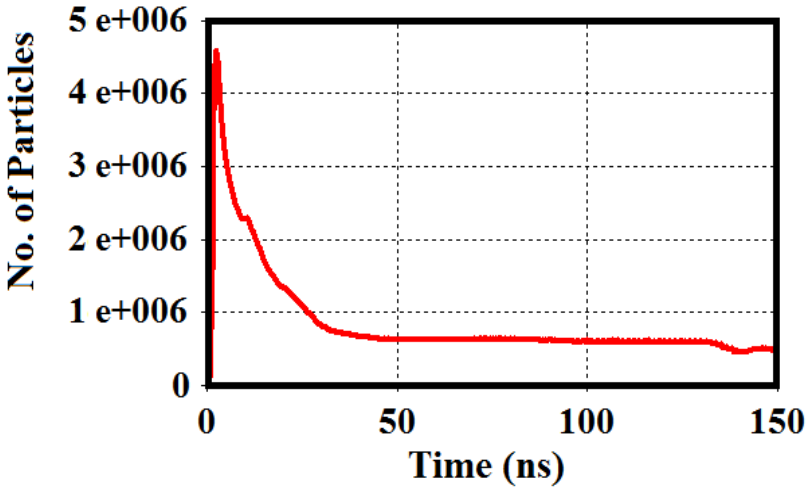


**Figure 6.23:** Number of particles emitted from the surface of the cathode structure at a different time in ns.

carried out using the PIC solver of 'CST Particle Studio'. The beam parameter for simulation is selected as: DC pulse beam voltage of 610 kV with 10 ns of rise time, 130 ns of hold time, and 10 ns of fall time and beam current of 58 kA. The input DC pulse voltage and generated current are shown in Fig. 6.22. With the application of input DC

pulse voltage between anode and cathode, the electron is emitted from the surface of the cathode through explosive emission. The number of electrons emitted from the surface of the cathode at different time instant is shown in Fig. 6.23.

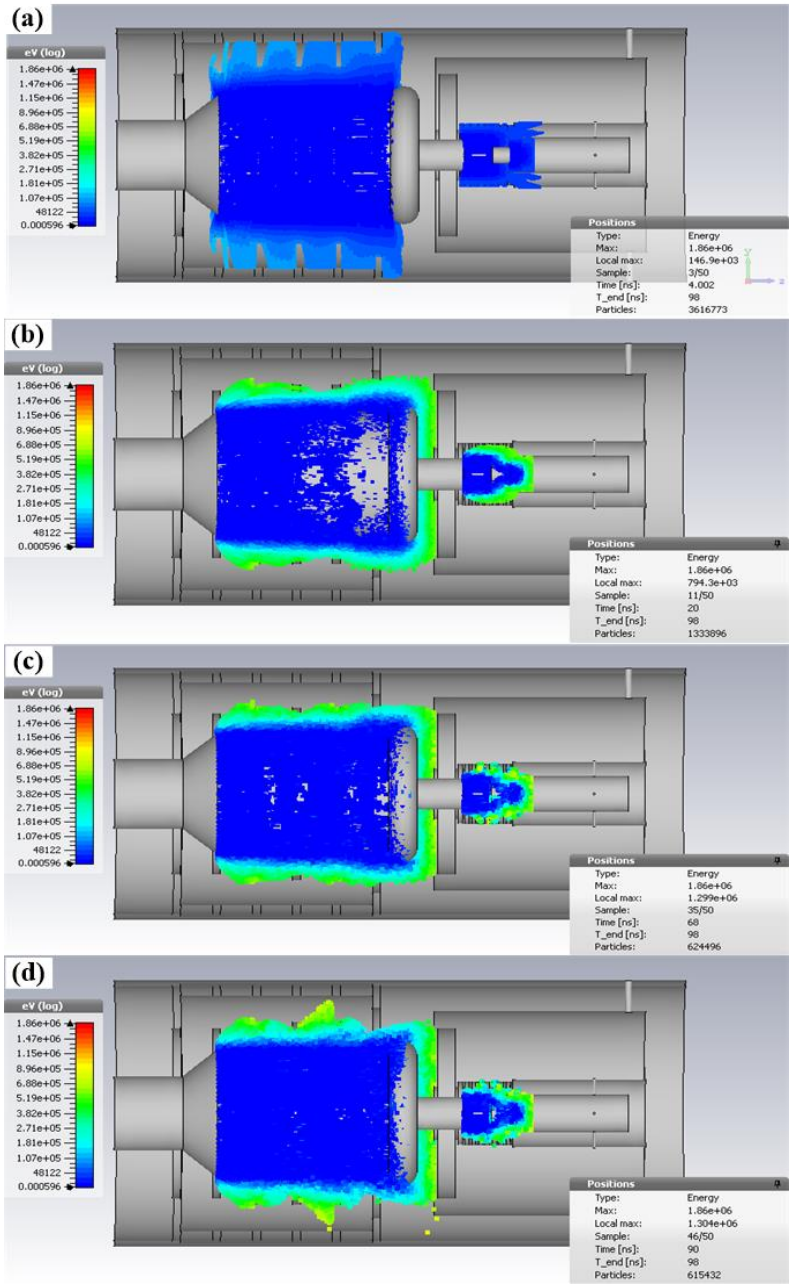


**Figure 6.24:** Different phases of beam wave interaction inside the device: (a) Pre-oscillation phase (b) magnetic insulation phase (c) start oscillation phase (d) non-linear phase.

The whole PIC simulation is divided into four different phases shown in Fig. 6.24. In the first phase, the emitted electrons from the cylindrical cathode surfaces (i.e. C1, C2, and C3) start moving towards the anode structure and are considered as pre oscillation phase as shown in Fig. 6.24(a). In the second phase, the self-magnetic insulation is taking place where the required critical current achieved by the current generated at load section (SWS2, C2, and C3), and this phase is considered as magnetic insulation phase which is shown in Fig. 6.24(b). After magnetic insulation, the third phase started in which an electron sheath is confined between the tip of the disc and cathode along the z-direction in both the SWS sections. The magnetically insulated electron sheath induces noise and creates diocotron instability inside the device to generate oscillation. The oscillation inside the interaction section starts when the drift velocity of electrons becomes equal to phase velocity supported by SWS cavities. This phase (i.e. the third phase) is called the start oscillation phase and is shown in Fig. 6.24(c). In the last phase which is shown in Fig. 6.24(d), the beam wave interaction taking place through the alternate formation of a spoke-like cloud between consecutive disc cavities called the non-linear phase. The axial electron motion excites the $TM_{01}$ mode inside the SWS structure with azimuthal symmetry in design. To track the axial motion of the electrons, an axial momentum tracker is applied during the PIC simulation with 10ns of tracking time steps. The absolute value of normalized momentum with respect to axial distance Z is shown in Fig. 6.25. It can be clearly seen from Fig. 6.25 that, the diocotron instability occurs inside the device forms $\pi$-mode (i.e. $180^0$ phase shift between consecutive cavity) of operation near both the interaction structure for efficient beam-wave interaction.

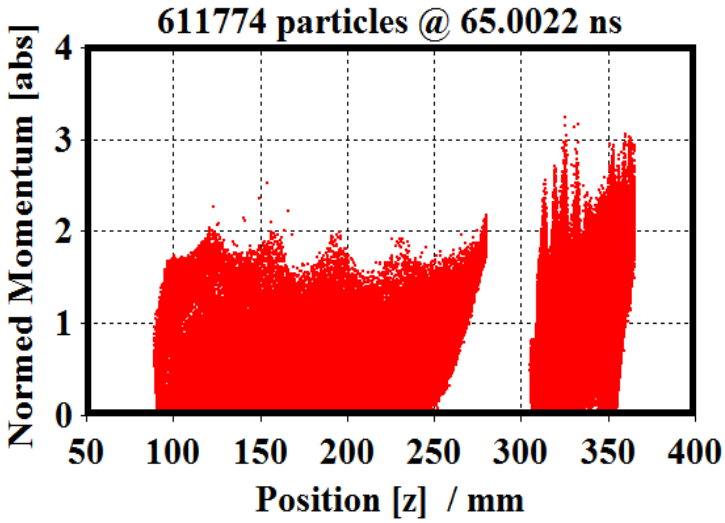


**Figure 6.25:** Normalized momentum at a different axial positions at 65.02 ns time of oscillation.

After the efficient beam-wave interaction, the RF signal generated inside the device is stored in the cavity (i.e. in the *S*-band section and *Ku*-band section) in the form of the standing wave. This stored energy is extracted out using different extractor section (i.e. extractor section-1 for *S*-band and extractor section-2 for *Ku*-band). The extractor section mainly changes the standing wave into the traveling wave and helps in matching the impedances between the interaction section and the output section. To track the generated RF signal, a waveguide port is placed at the output section-1 (i.e. for *S*-band) and output section-2 (i.e. for *Ku*-band). The RF signal and its frequency spectrum received at the waveguide port at section-1 are shown in Fig. 6.26. Fig. 6.26(a) shows the RF signal amplitude with respect to time whereas Fig. 6.26(b) shows the FFT (Fast Fourier Transform) of the received signal. It can be seen from Fig. 6.26(b) that the received RF signal at section-1 having 2.098 GHz frequency (i.e. in *S*-band) and verify our expected design parameters. Similarly, a waveguide port placed at output section-2 observes the generated signal at the second interaction structure (i.e. for the *Ku*-band

generation section). Fig. 6.27(a) shows the RF signal amplitude with respect to time whereas Fig. 6.27(b) shows the FFT of the received signal. It can be seen from Fig. 6.27(b) that the received RF signal at section-2 having 13.947 GHz frequency (i.e. in *Ku*-band) and verify our expected design parameters. The drop in the frequency at the higher band is due to the beam loading effect and corner effect of disc loading. The beam loading effect and disc corner effect does not impact much for the lower band.

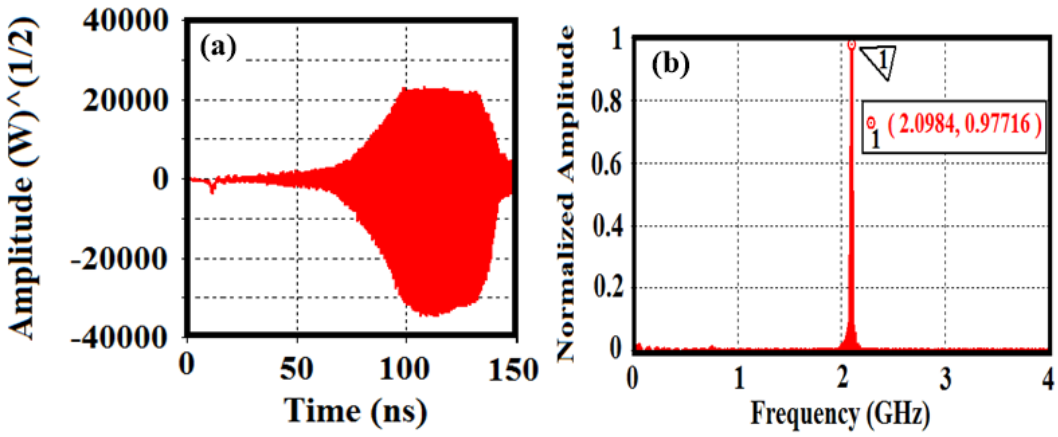


**Figure 6.26:** *S*-band (a) received RF signal at the output port (b) frequency spectrum of corresponding RF output signal found through Fast Fourier Transform (FFT).

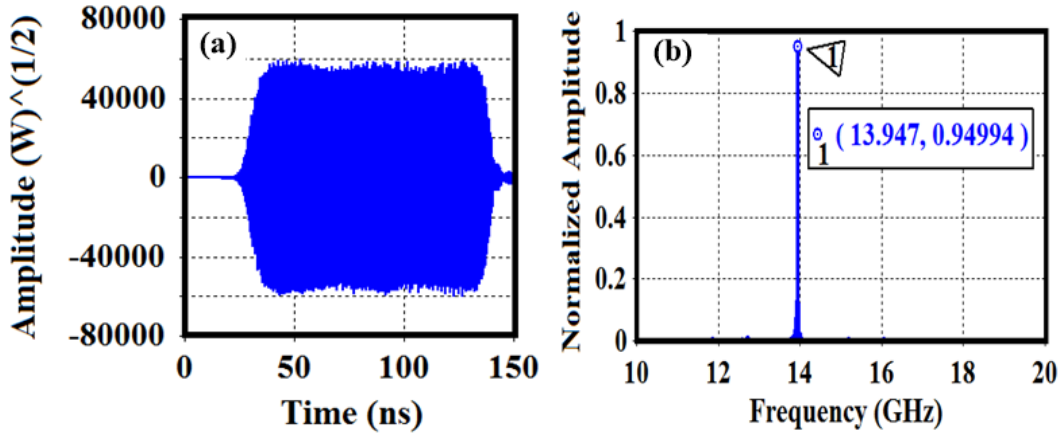


**Figure 6.27:** *Ku*-band (a) received RF signal at the output port (b) frequency spectrum of corresponding RF output signal found through Fast Fourier Transform (FFT).

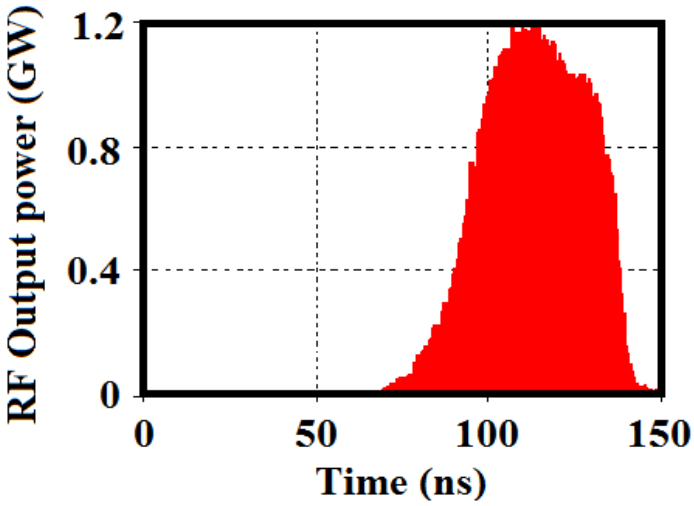


**Figure 6.28:** RF output peak power (in GW) received at the output port for *S*-band.

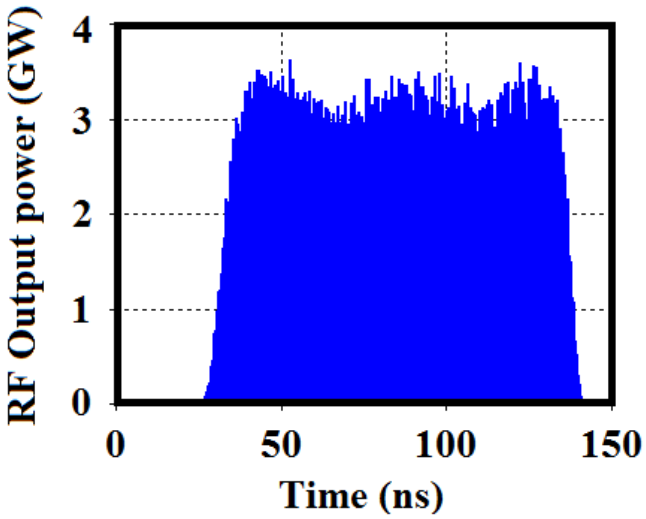


**Figure 6.29:** RF output peak power (in GW) received at the output port for *Ku*-band.

The RF power calculated for *S*-band signals is shown in Fig. 6.28. It can be seen from Fig. 6.28 that, the peak RF power generated for *S*-band is ~ 1.2 GW but its pulse is very narrow. The reason behind this problem is that the instability that arises near the *S*-band section takes a long time with respect to that near the *Ku*-band interaction section. The RF power calculated for *Ku*-band signals is shown in Fig. 6.29. It can be seen from

Fig. 6.29 that, the peak RF power generated for *Ku*-band is ~ 3.1 GW. Thus, with the application of beam parameters of 610 kV voltages and 58 kA current the particle simulation provides ~3.1 GW RF output power in *Ku*-band and ~1.2 GW RF output power in *S*-band with an overall efficiency of ~12.1%.

## 6.5 Conclusion

In this chapter, different bi-frequency MILO (i.e. *L*-band bi-frequency MILO and *S*-band bi-frequency MILO) along with dual-band MILO (i.e. MILO which generate RF power in *S*-band and *Ku*-band simultaneously through different interaction structures) have been designed and investigated using analysis and further the designed device is validated through PIC simulation using a commercial code. The design expression is derived for calculating the different design parameters for different bi-frequency MILO. The beam wave interaction process has been explained and the temporal growth rate calculated numerically for dual-band MILO. Analytical computations approach has been used to find the dispersion curve and validated using eigenmode simulation for different interaction structures for *L*-band and *S*-band bi-frequency MILO and for *S*-band and *Ku*-band related to dual-band MILO, respectively. Finally, the PIC simulations have been performed for different designed bi-frequency MILOs. The *L*-band bi-frequency MILO device performance evaluated with the typically selected beam parameters: diode voltage of 420 kV and diode current of 38 kA and RF signal generated at two modes has been obtained at the output with combined RF peak power of ~1.29 GW. The overall efficiency of ~8% was obtained through the *L*-band bi-frequency MILO device. After the validation, a beam dump disc was used for reuse of electron beam present in collector results performance improvement by enhancing efficiency to ~9.8%. Similarly, S-band

bi-frequency MILO generated RF signal at two frequencies and combined RF peak power of ~2.86 GW and average power of ~1.43 GW is obtained at the output with the application of typically selected beam parameters: diode voltage of 490 kV and a diode current of 45 kA. The overall efficiency of ~6.5% was obtained through the *S*-band bi-frequency MILO. Finally, the PIC simulation for dual-band MILO was used with the application of 610 kV voltages and 58 kA current and generates 3.1 GW RF power in *Ku*-band and 1.2 GW RF power in *S*-band with the overall efficiency of ~ 12 %.